Additive manufacturing of 17–4 PH steel using metal injection molding feedstock: Analysis of 3D extrusion printing, debinding and sintering

Gurminder Singh, Jean-Michel Missiaen, Didier Bouvard, Jean-Marc Chaix

Additive Manufacturing 47 (2021) 102287

Contents lists available at ScienceDirect

Additive Manufacturing

journal homepage: www.elsevier.com/locate/addma

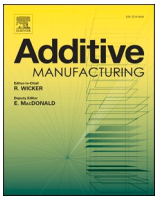

Research Paper

Additive manufacturing of 17–4 PH steel using metal injection molding feedstock: Analysis of 3D extrusion printing, debinding and sintering

Gurminder Singh [a,b,*], Jean-Michel Missiaen [a], Didier Bouvard [a], Jean-Marc Chaix [a]

[a] CNRS, Grenoble INP, SIMAP, University Grenoble Alpes, 38000 Grenoble, France
[b] School of Mechanical & Materials Engineering, University College Dublin, Belfield, Dublin 4, Ireland

ARTICLE INFO

Keywords:
3D extrusion printing
Metal injection molding
Debinding
17–4 PH Steel
Sintering

ABSTRACT

The amalgamation of 3D extrusion printing (3DEP) and sintering results in a low-cost process compared to other laser-based additive manufacturing techniques. This work used metal injection molding (MIM) raw material of 17–4 PH steel for additive manufacturing. The 3D printing, debinding, and sintering steps were thoroughly evaluated to achieve the highest sintered density. First, the 3DEP of the MIM feedstock was carried out using a screw-based extrusion system at optimum parameters to acquire the high green density and fine surface roughness. The solvent debinding step was carried out on 3D printed samples to remove water-soluble polymer by immersion method. Thermogravimetric analysis was performed to evaluate the decomposition temperature of the backbone material. Further, thermal debinding and sintering steps were conducted in a single step. The thermal debinding temperature was 500 ℃, and the sintering temperatures were chosen as 1100, 1200, 1300 and 1360 ℃. The highest density of ~95.6% was attained at a high sintering temperature. The micro-tomography evaluation was carried out on the 3D printed green and high-density sintered samples to evaluate the internal porosity. The mechanical properties and the microstructure were also evaluated for sintered samples. The work opens a way to fabricate metal complex-shaped parts at low cost using market available MIM feedstock.

1. Introduction

In the past two decades, development innovations, which dramatically shorten the period between design and finished parts, have gained substantial attention because of the availability of digital design instruments. This refers to additive manufacturing (AM), where the products are fabricated by adding material layer-by-layer [1]. The popular AM processes are selective laser melting (SLM) and electron beam melting (EBM), in which the powders are added layer-by-layer or at a specific area and melted using either a high-energy laser or an electron beam [2,3]. In these direct AM processes, the parts are fabricated layer-by-layer in one step, and the excess unconsolidated power is simply blown out. Other AM processes such as binder jetting [4,5], rapid tooling [6–9], stereolithography [10–12] and 3D extrusion printing (3DEP) [13] combined with sintering require more than one step for the fabrication of metal/ceramic parts. These processes require a longer processing time to fabricate a solid part, but they are cheaper than direct processes in initial investments, equipment, and skilled labor costs. They could be implemented on an industrial scale by improving a few characteristics. This introduces the need for an affordable AM production system where the metal samples can be made quickly at low cost with design and material freedom and, possibly, upgradable to mass production like the metal injection molding process (MIM).

Mass-production of powder metallurgical components is typically achieved in MIM. It includes a few steps: feedstock preparation, injection molding, debinding and sintering [14]. The MIM process blends polymer molding geometric versatility with metal-related properties such as excellent mechanical, thermoelectric, magnetic and electrical properties. The optimization of feedstocks implies designing suitable binding polymers and modifying powder properties. The particle size, for instance, is a critical factor in achieving MIM efficiencies like high relative density, microstructure and mechanical properties. Nowadays, MIM-like feedstock is being used in the fused filament fabrication (FFF) AM process to fabricate the green body. Later on, debinding and sintering steps are performed similarly to the MIM process to obtain metal parts. The FFF process is commonly used to print thermoplastic materials using a 3 mm or 1.75 mm polymer filament wire. The wire is extruded from the nozzle near its melting point on a hotbed and the part is printed layer-by-layer in 3D following a CAD model. However, to fabricate metal-polymer parts similar to MIM injected parts, a particular

* Corresponding author at: CNRS, Grenoble INP, SIMAP, University Grenoble Alpes, 38000 Grenoble, France.
E-mail address: Gurminder.singh@ucd.ie (G. Singh).

https://doi.org/10.1016/j.addma.2021.102287
Received 21 May 2021; Received in revised form 11 August 2021; Accepted 31 August 2021
Available online 10 September 2021

type of filament feedstock is required. Feedstocks, though with higher viscosity, can be treated similarly to regular polymers. The flowability inevitably restricts powder loading to a maximum of 55–65 vol%. In recent times, many authors have shown interest in developing metal filament for the FFF process. Ren et al. [15] used copper particles, paraffin wax, stearic acid and low-density polyethylene for the to develop metal filaments and optimized the printing parameters to obtain high tensile strength in the green part. Later on, debinding and sintering steps were performed on the green part to obtain the final copper parts with 8.15 g/cm^3 density. Gonzalez-Gutierrez et al. [16] prepared a filament of SS 316 alloy with binders for the 3D printing of the green part. The debinding steps were performed with different parameters to remove a maximum binder and obtain defect-free sintered parts. Similarly, Gonzalez-Gutierrez et al. [17] used a combination of grafted polyolefin, thermoplastic elastomer and 17–4 PH particles for the filament preparation and processed green parts for tensile test specimen by FFF. The debinding and sintering steps were performed to obtain solid steel specimens, resulting in 96.5% relative density. Rane et al. [18] used a water-soluble binder (Embemould K83) and SS316 metal particles to extrude the green parts. The surface quality was investigated by parametric variations. The layer height was the dominating parameter for the surface quality rather than the extrusion speed, the table speed and the hatching spacing. Thompson et al. [19] also used thermoplastic elastomer and polyolefin binders and SS 316 metal particles for filament preparation. 3D printed green parts were further used for the debinding and sintering steps. Sintered parts with 95% density were obtained. Many other authors explored the FFF fabrication process of metal or ceramic binder filaments for different materials such as copper [20], SS 17–4 PH [21,22], SS 316 [23,24], Zirconia [25,26], Alumina [13], etc. Many companies are providing commercial metal filament wires for the FFF processes. The UltraFuse 316 LX filament is one example explored by Gong et al. [21] for printing SS 316 solid parts. Some companies developed in the last few years, such as Desktop Metal and Markforged, now provide complete raw material, 3D printing machine, debinding and sintering equipment. These commercially available machines also use extrusion of MIM-like feedstocks for printing. However, they have named their technologies differently as ADAM (atomic diffusion additive manufacturing) [27] for Markforged and BMD (Bound Metal Deposition) [28] for Desktop Metal. These companies provide feedstocks for different types of materials such as Inconel 625, Ti6Al4V, D2 steel, etc. The 3DEP AM process with sintering is cheaper as compared to the direct AM process in the initial investment, equipment, and labor cost. Also, it required small amount of material to process at a moment as compared to other powder-based AM processes. The properties obtained from this method could compete to the traditional powder-based AM and MIM processes.

The studies mentioned above need special preparation for the material feedstock for extrusion printing. The entire extrusion process is optimized, beginning with the raw materials determined by the metal particle size and shape and the binder composition. The fabrication of filaments or customized feedstocks results in a high cost for the whole process. On the contrary, MIM feedstock granules, commercially available on the market, are cheaper and designed in terms of binder type and composition to achieve highly dense sintered parts. MIM feedstock granules can also be used directly for the 3D printing of green parts using screw extruders instead of preparing filament wire for the printing. Singh et al. [29,30] explored the 3DEP process using direct market available MIM copper feedstock granules. The effects of 3DEP parameters such as extrusion temperature, nozzle speed, extrusion multiplier and layer height were explored for the green density and surface roughness using MIM copper feedstock [29]. 3DEP parameters have shown a significant effect on roughness and green density. The overall process was optimized to achieve maximum density and minimum surface roughness of the 3D printed green parts. The tomography analysis revealed the importance of optimization for 3D printing to achieve minimum porosity at the green stage of the process. Further stages such as debinding and sintering, similar to the MIM process, were highly contributed to achieving high copper solid density [30]. The work possessed the requirement of parameters study at different stages, such as at debinding to remove the maximum amount of polymer and at sintering to achieve maximum density. Only density study with tomography analysis was performed for the copper MIM feedstock. The mechanical properties have not been reported. Also, Lengauer et al. [31] used a similar type of market available WC-Co MIM feedstock for the 3D extrusion printing. Only two market accessible MIM materials, namely copper and WC-Co, have been explored in the literature for 3D printing, debinding and sintering. Therefore, studies are needed to explore the different MIM granule feedstocks' feasibility as raw material for 3D printing. The present study aims at exploring additive manufacturing of SS 17–4 PH MIM feedstock granules. The 17–4PH steel is hardened steel, having a wide variety of applications in manufacturing machinery, chemical processing, jigs and fixtures, valving, fasteners, and pump components. The involvement of different materials composition makes it more complex to fabricate with high density and get a better surface finish. To compete with the traditional MIM process to eliminate the requirement of dies for complex shapes, the in-depth analysis of each step is required for 3DEP of 17–4PH steel MIM feedstock. In the present study, screw-based 3DEP was used to 3D print green samples of 17–4 PH steel MIM feedstock. Furthermore, a solvent debinding step was explored to remove water-soluble polymer. To acquire high-density samples, thermal debinding and sintering procedures were carried out together. Additionally, the tomography and SEM analysis have been performed at different steps to investigate the porosities. The overall parameters of each stage have been identified to obtain high solid density with minimum porosity. The mechanical test to obtain hardness and tensile properties have also been conducted. Later, the acquired properties have been tried to compare with the literature of 17–4 PH material fabricated from another additive manufacturing and MIM process routes.

2. Materials and methods

The workflow diagram used for the additive manufacturing of 17–4 PH steel is shown in Fig. 1. The details of each step are discussed in the following sections.

2.1. Materials

The market available SS 17–4 PH MIM raw material was procured from PolyMIM (Germany) and was directly utilized for 3D printing. SEM pictures of the granules are shown in Fig. 2(a) and 2(b). The metal particle size is in the range of 2–10 μm from these images. The composition of the SS 17–4 PH alloy is shown in Table 1. A TGA test was performed to investigate the weight of the binders in the feedstock. The sintering kinetics of 1℃/min heating rate up to 500 ℃ temperature for 1 hr heating time was used for TGA test. A total weight loss of 6.5 ± 0.2% was measured (ref. Fig. 2(c)). Two main steps as per derivative of weight were observed in relation to the different types of binders in the feedstock. Generally, polyMIM feedstock consists polyethylene glycol (PEG) and some wax (supplier did not provide details) [32]. The first degradation ramp could be related to the low molecular weight binder, and the second could be related to the high molecular weight binder [33]. The feedstock has been commercially made for the MIM process and designed to have required yield stress, shear-thinning behaviour and viscosity (below 1000 Pa s in the shear range of 102–105 s^{-1}) for the injection process [34]. These properties give the advantage to use MIM feedstock for 3D printing using an extrusion-based system. The 3D printing process required nearby similar behaviour of the material for the extrusion [35]. Other advantages are providing strength to the printed part, and the binders of polyMIM feedstock are easy to remove by solvent and thermal debinding steps. Later, sintering of the parts could provide the density, shrinkage, and

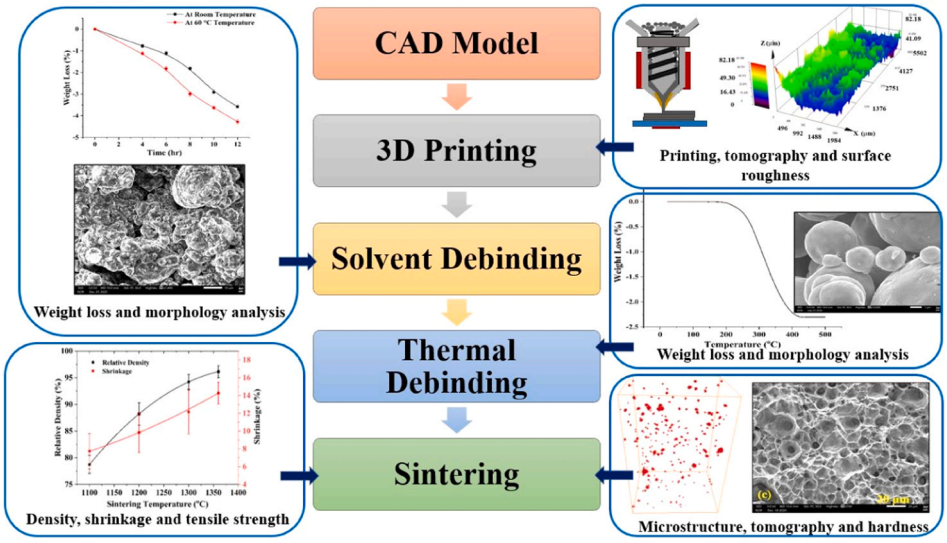

Fig. 1. Process flow diagram for additive manufacturing of 17–4 PH steel.

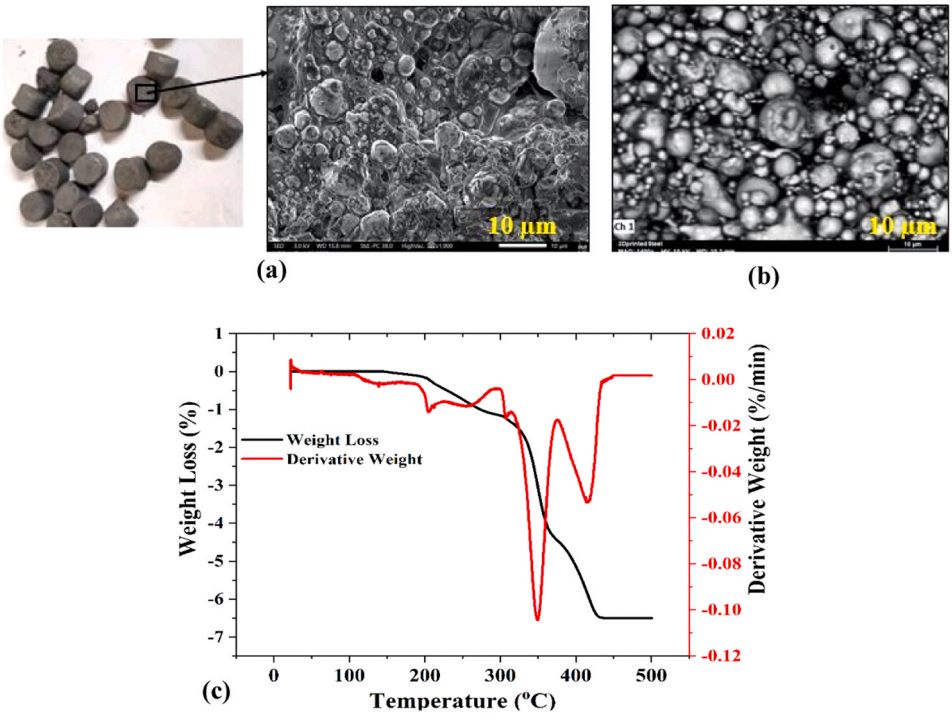

Fig. 2. (a) SEM, (b) backscattered image and (c) TGA analysis of SS 17–4 PH MIM feedstock.

Table 1
Composition of 17–4 PH alloy (provider's data).

Element	Fe	Cr	Ni	Mn	Si	Cu	C	Nb	O	P	N
Composition (%)	Balance	16.4	4.97	0.49	0.53	4.29	0.037	0.43	0.062	0.024	0.078

other properties like MIM process fabricated samples. However, the limitation of the MIM feedstock for 3DEP is to maintain homogeneity during printing. The low volume of feedstock in the extruder could print uneven amount of filament material.

2.2. 3D Printing

The part was modeled by CAD (computer-aided design) using SolidWorks software and converted into a tessellated file. Simplify3D software was used to slice the tessellated file. The sliced part was saved as a Gcode file for communication to the 3D printing machine. A screw-based 3DEP apparatus (Exam 255) from AIM3D (Germany) was

employed to manufacture green parts using MIM feedstock. The printer can be used to fabricate volumes up to 255 × 255 × 255 mm^3. The 3D printing machine with a schematic illustration is shown in Fig. 3. The uniqueness of the setup is the compact screw-extruder for thermo-mechanical deformable materials [36]. The screw extruder has a significantly smaller length-to-diameter ratio and located in the funnel-shaped infeed region of the vertically arranged extruder, which prevents rotational movement of the material in the funnel. Also, it forces movement in the screw extruder's conveying direction in combination with the gradients of screw flanks. Furthermore, the material is crushed, increasing the bulk material density in the screw area and the material is extruded from the nozzle.

A pneumatic controlled piston ("faker") was employed for the smooth feed to the screw extruder. Heaters were used to adjust the extrusion temperature for smooth printing. The material was extruded using a standard FFF hardened steel nozzle of 0.4 mm outlet diameter with 13 mm length and 3 mm inlet diameter. The material was fed from the top of the extruder and extruded from the nozzle. The binders of the MIM feedstock provided the required flowability for the hot extrusion as discussed above. The melted binders of MIM feedstock and metal particles deposited on the hot bed layer-by-layer like FFF process and adhered to each other in melted stage. The printing parameters used for the present study were adopted from the previous study of parameters optimization for copper MIM feedstock by Singh et al. [29]. The experiments were designed to achieve optimal printing parameters to maximize green density, eliminating voids and achieving the lowest possible roughness. The central composite design method was used to design the set of experiments. The response surface methodology was applied to develop quantitative relationships in regression equations between the parameters mentioned above for green density and surface roughness. The interactions between the parameters were also studied. Further, multi-objective optimization based on genetic algorithm was used to optimize the parameters to obtain maximum green body density and minimum surface roughness. The obtained optimum parameters were: 0.05 mm layer-thickness, 20 mm/sec nozzle-speed, 120% extrusion (extruder flow), 196 °C extrusion-heating temperature, 60 °C bed temperature and 100% infill-density. The extrusion temperature has been found to be nearby recommended temperature (195 ℃) for the injection molding of polyMIM material [34]. These printing parameters are assumed to result in optimum green density and roughness for the current study of 17–4 PH MIM feedstock due to identical polyMIM binders.

2.3. Debinding and sintering

To extract all binders from the green body, the debinding process was done in two stages: solvent and thermal debinding. For PEG extraction, solvent debinding was used. The samples were submerged in water and magnetically stirred for 12 hr at room temperature and at 60 °C temperature. Further, specimens were dry for 2 hr in a thermal oven at 100 °C. Samples were weighed before and after drying, and the weight loss was estimated. The weight was calculated after 4, 6, 8, 10 and 12 hr of immersion at room temperature and at 60 °C temperature. Three sets of experiments were performed for both conditions. The average along with the standard deviation were calculated. A thermogravimetric (TGA) preliminary study in the He-4% H_2 atmosphere has been carried out to evaluate the thermal debinding temperature. The blank test was performed for each TGA test to remove the error from the data. Thermal debinding and sintering steps were performed in a tube furnace in a single thermal cycle: 1 °C/min heating rate up to thermal debinding temperature (500 °C), 1 hr of soaking time, 4 °C/min heating rate to different sintering temperatures with 5 hr soaking time and 4 °C/min cooling rate to 20 °C in He-4% H_2 atmosphere. The sintering temperatures were chosen as 1100 ℃, 1200 ℃, 1300 ℃ and 1360 ℃.

2.4. Characterization

The cylindrical samples with size (4 mm ∅ and 4 mm height) were fabricated for the characterizations. Scanning electron microscopy (SEM) images at various processing stages were captured with the JEOL-JSM-IT-500-HR machine. The mass and volume of 3DEP specimens are used to calculate the green density. The volume was calculated from the geometrical dimensions measured with a Vernier caliper with the least count of 0.01 mm, and the mass was measured using a weighing scale with 0.001 g least count. The shrinkage percentage concerning CAD model was estimated using cylindrical samples. Following ISO 4287, the sample roughness was measured in the printed direction using an Olympus (DSX 500) digital microscope. The weight density of sintered samples in air and ethanol was measured using a three-mass Archimedes system. The sintered samples' relative density was calculated using the theoretical density of SS 17–4 PH. The Vickers scale was used to determine the sample's hardness. The samples' hardness was measured at various points, and the average of the measurements and the standard deviation were calculated. The tensile specimens were prepared according to ASTM standard B925–15 and the test was performed at a

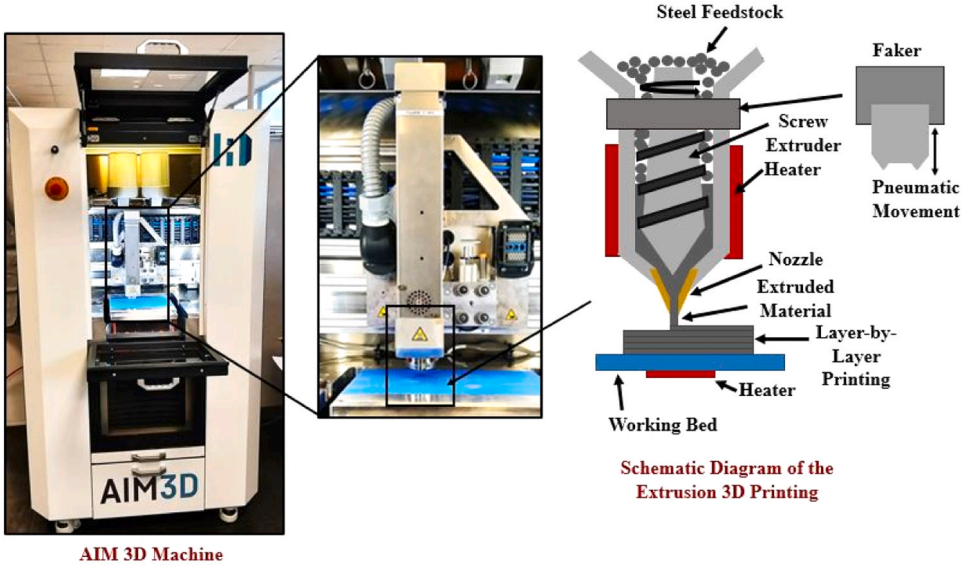

Fig. 3. Schematic diagram and picture of the Exam 255 3D printing machine from AIM3D™.

speed of 1 mm/min on a standard tensile testing machine at room temperature with static condition. Emery paper with grits varying from 180 to 4000 was used to grind the sintered samples. To achieve a mirror-like finish, further polishing was done with 6 μm and 1 μm diamond paste. The polished sample was etched with a mixture of 15 mL glycerin, 10 mL HCl, and 5 mL nitric acid, as per ASTM standard E407–07. An Olympus DSX500 microscope was employed for the examination of etched specimens. The samples were observed in microtomography (μCT) using Easytom-XL based machine. This test used 150 kV and produced images with 4.2 μm voxels. For image processing, the programs ImageJ and Avizo Lite were employed. By thresholding, the voids or pores were extracted in ImageJ. As explained below, voids correspond to extrusion or printing defects in the green body, whereas pores refer to the empty spaces left after debinding and sintering. Following thresholding, the voids/pores were separated and connected in 3D using the Boulos et al. [37] algorithm. From the segmented data, the volume (V) and surface area (A) of every void/pore were evaluated. Eqs. (1) and (2) were used to calculate the equivalent diameter (d_{eq}) and sphericity (S). Sphericity is a number that ranges from 0 to 1, with 1 denoting a sphere.

$$d_{eq} = 2 \times \left(\frac{3 \times V}{4 \times \pi}\right)^{1/3} \quad (1)$$

$$S = 6 \times V \times \left(\frac{\pi}{A^3}\right)^{1/2} \quad (2)$$

3. Results and discussion

3.1. 3D printing

The SEM view of 3D printed green part in the direction of printing is shown in Fig. 4(a). Two types of voids, namely extrusion and printing voids, are visible in the 3D printed part. The extrusion voids on the extruded material surface were generated by the stresses experienced by the granules during screw extrusion. Surface cracks are also observed along with the extrusion voids. Printing voids also formed between the printing layers. Both types of voids directly depend on the values of the 3D printing parameters. The significant parameters affecting the 3D printing quality are extrusion temperature, layer thickness, extrusion multiplier and nozzle speed. The effects of these parameters for a copper MIM material comprising similar binders were discussed in the previous study [23] for the green body density and roughness. As mentioned earlier, the same parameter values were used for the present study of SS 17–4 PH MIM material. The green density value of the fabricated samples was ~4.91 g/cm^3. The high magnification SEM image of the green body is shown in Fig. 4(a). The binder can be identified between metal particles. Fig. 4(b) depicts the surface roughness in 2D and in 1D (line plots) of the green body in the printing direction. Green bodies with ~2.7 μm surface roughness value with uniform distribution of waviness were obtained by using optimized printing parameters.

Tomography was used further to investigate the internal voids in the green body. The different phases of the material, such as metal particles, binders and voids, could be visualized from the μCT. For the interest of the present study, only voids were extracted by thresholding. Fig. 5(a) shows a 3D rendering of the μCT results, with thresholder voids highlighted in red. The volume fraction of voids was determined to be ~1.6% in the printed sample, with an average void diameter of 13 μm. Fig. 5(a) and 5(b) indicate the frequencies of the diameter and sphericity of the voids. The voids were found to be of small size, measuring less than 35 μm in diameter. Long chains of voids, which would have been characteristic marks of poor deposition during 3D printing, are not observed. Voids are observed to be roughly spherical and randomly dispersed. These voids could be extrusion voids and small printing voids, which are nearly impossible to eliminate.

3.2. Solvent and thermal debinding

The solvent debinding step was used to remove water-soluble polymer, i.e., PEG from the 3DEP green body. The samples were submerged in water at different temperatures for different times. The immersion time impact on weight loss (%) at different temperature is shown in Fig. 6(a). The dissolution rate in water is slow at the beginning of the

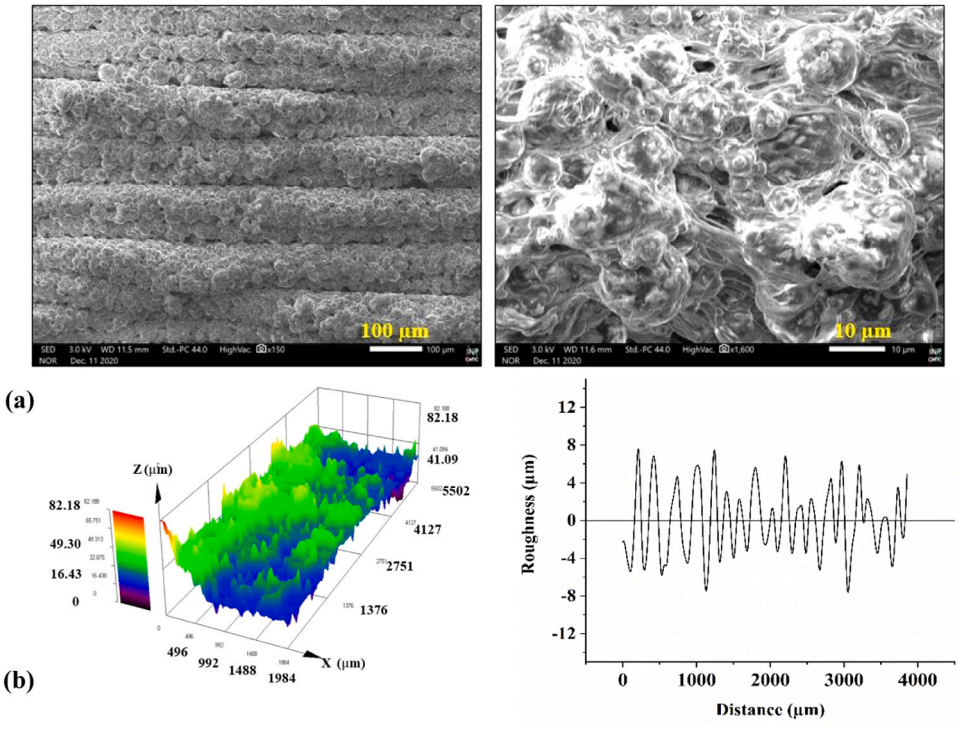

Fig. 4. (a) SEM images, (b) surface profiles of the 3D printed sample.

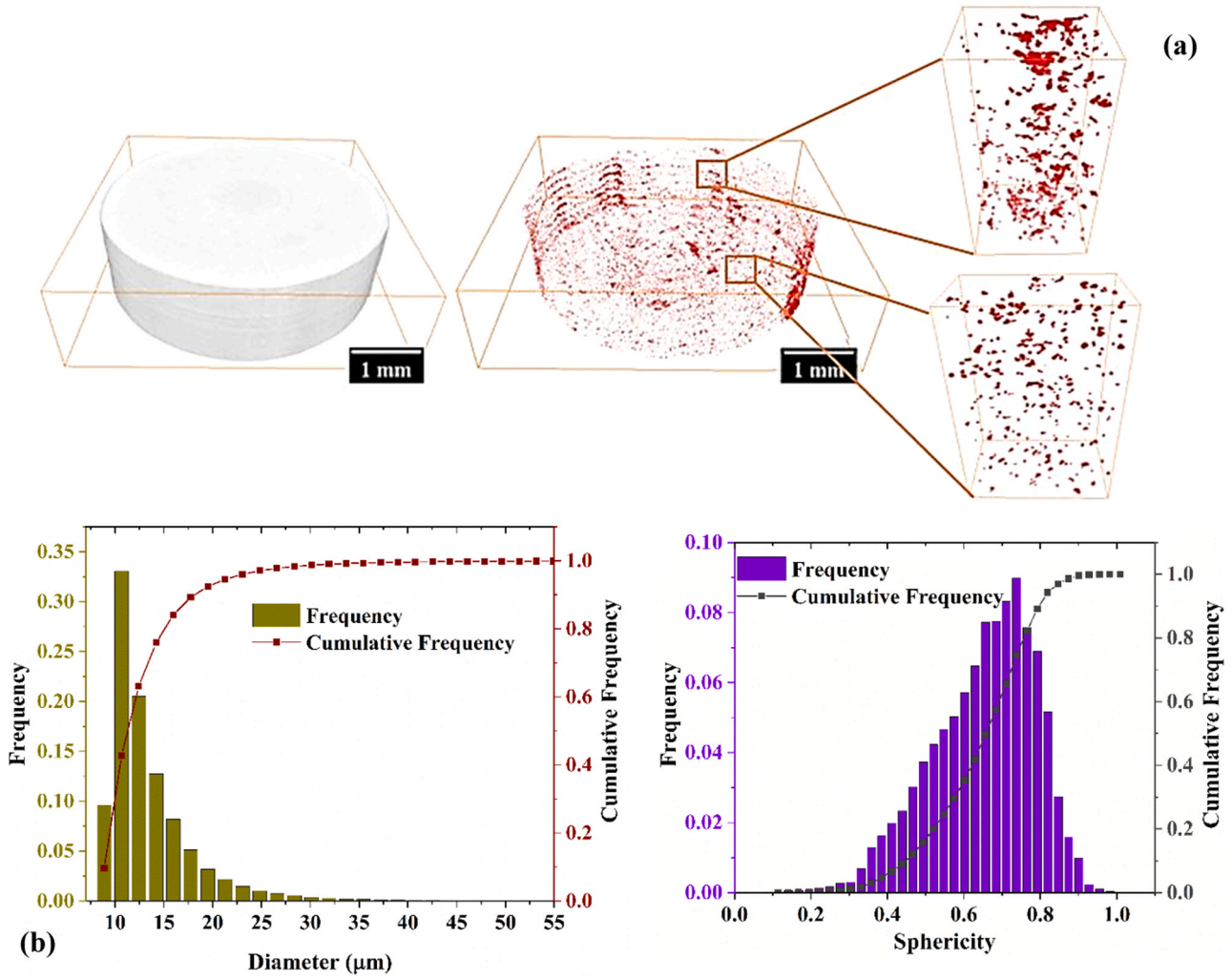

Fig. 5. (a) 3D rendering of tomography data with thresholded voids in red, (b) voids size distribution and (c) sphericity distribution of 3D printed sample.

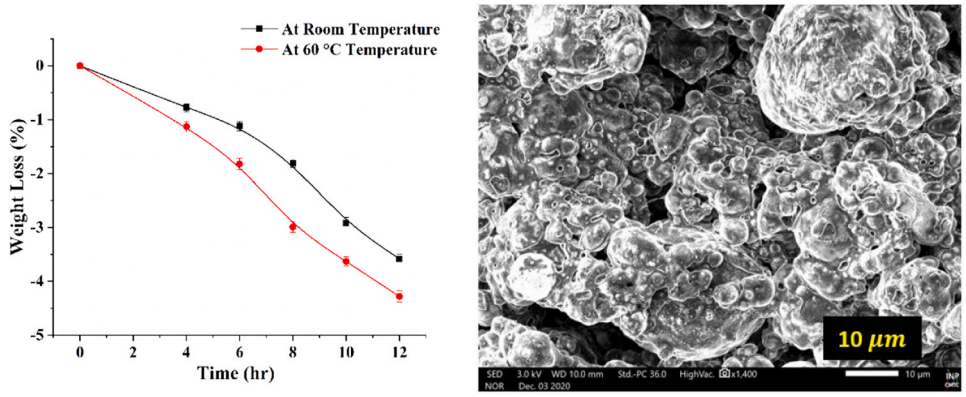

Fig. 6. (a) Green body weight loss through solvent debinding process and (b) SEM view of the solvent debinded sample.

immersion period until 6 hr. However, with increasing immersion time, the rate of dissolution increases rapidly until 11 hr. The polymer dissolved at the beginning of the immersion probably forms channels, which later help the internal polymer to dissolve. The weight loss rate in water at 60 ℃ is higher compared to the room temperature. The polymer hydroxide bonds broke faster at 60 ℃ temperature when approaching the melting point of PEG as compared to room temperature. The maximum weight loss was identified as ~4.4% at 60 ℃ temperature after 12 h of immersion. The change in weight after 12 h was insignificant.

PEG was believed to be fully soluble in water. The removal of PEG can be identified after drying the sample (Fig. 6(b)). The backbone polymer or wax can be seen holding metal particles. The strength of the backbone polymer was enough to take out the sample from the beaker and to place it in the oven and further in the furnace. The formation of interconnected voids can also be observed, allowing the diffusion of

gaseous decomposition products during thermal debinding.

A thermogravimetric (TGA) test was performed on the solvent debinded sample to confirm the full removal of PEG during solvent debinding and to quantify the weight loss percentage via the thermal debinding procedure. Fig. 7(a) represents the TGA curve of the solvent debinded sample with 1 ℃/min heating rate up to 500 ℃ with 1 h holding time. A single step was identified during mass loss, which probably represents backbone polymer or wax. The solvent debinding parameters were then correctly adjusted to remove most of the PEG. ~2.25% weight loss was measured during TGA. The SEM image after TGA depicts only metal particles that are free from binders (Fig. 7(b)). Without solvent debinding, the immediate thermal debinding and sintering of the green sample were also attempted. The high amount of binder formed cracks in the sample during extraction in thermal debinding. Therefore, the solvent debinding is necessary to extract part of the binder before thermal debinding and sintering to get a defect-free sintered sample. The thermal debinding to remove backbone polymer and sintering to densify metal particles were carried out in a single thermal treatment after solvent debinding.

3.3. Sintering

After thermal debinding, the specimens were sintered at different temperatures, i.e. 1100, 1200, 1300, and 1360 °C. Fig. 8 depicts the influence of sintering temperature on relative density and shrinkage (a). If the sintering temperature rises, the relative density increases as well. The highest relative density of ~96.5% was measured for the sample sintered at 1360 °C. The microstructures of the samples are shown in Fig. 9. The geometrical changes in the porosity concerning temperature can be easily identified in the microstructure. A large number of pores at 1100 ℃ is consistent with the low density of ~78.2%. The powder particles in the sintered sample have formed a skeleton after being interconnected by sinter bonds (Fig. 9(a)). Further, increasing the sintering temperature up to 1200 ℃, the pore structure becomes tubular and rounded, and the discrete particles are less evident. This is visible in the microstructure of the sample sintered at 1200 ℃ (Fig. 9(b)).

Further increasing the temperature up to 1300 ℃ induces a considerable reduction of the porosity. According to the literature, in the light of the ternary iron-chromium-carbon phase diagram, a new phase known as δ-ferrite, a solution of iron, carbon, and other alloying elements with a bcc composition, will form. [38]. The new phase develops with a regular shape and increases in size and quantity. The formation of δ-ferrite starts between 1270 and 1300 ℃ and strongly enhances sintering [39,40]. Its formation depends upon the powder chemical composition, sintering temperature, and also on the amount of residual carbon left by polymer binders after thermal debinding. It has also been shown that when δ-ferrite grows at high temperatures, the porosity reduces quickly, and the pores spheroidize and close [40]. More interestingly, as the pores come into touch with the δ-ferrite, they tend to shrink quicker [41,42]. Fig. 9(c) and (d) show that several of the existing spherical pores are situated inside the matrix, apart from the δ-ferrite, suggesting that this phenomenon is plausible. As a consequence, the existence of δ-ferrite at the pore surface can facilitate pore shrinkage. The densification and microstructure formation were similar to existing MIM 17–4PH studies [39,43–45]. However, a small number of intragranular pores is still present at 1360 °C, which is further analyzed by the tomography test.

The shrinkage in the samples was isotropic in nature. The maximum shrinkage was ~14.2% at the highest temperature. To achieve equivalent dimensions throughout the sintered sample as the CAD model, a geometry compensation of ~16.5% in each direction should be added to the CAD model dimensions during slicing procedure. The sintered sample with the maximum density had a surface roughness of ~3.6 μm. This value is greater than the green body's surface roughness (2.7 μm). Due to sintering, the sample's surface roughness can rise due to shrinkage and the forming of surface pores. In the future, a more in-depth investigation of the relationship between 3D printing and sintering parameters and surface roughness would be needed.

Fig. 8(b) depicts the change in Vickers hardness of the sintered sample concerning sintering temperature. Initially, the hardness increases due to a reduction in porosity with temperature, as discussed above. However, with increasing temperature beyond 1200 ℃, the change in hardness value is insignificant, although the porosity still decreases. This may be due to a compensation of positive effect of porosity elimination by the negative effect of grain growth or the heterogeneity in pore distribution between surface and bulk, as noticed in [39,40].

A tomography scan of the sample with high density was performed in order to investigate the inner porosity of the sample. Fig. 10(a) describes a 3D rendering structure of porosity after processing. The volume fraction of porosity was estimated to be ~2.1%. This is lower than the 3.5% estimate derived from relative density. This is attributable to the 4.2 μm voxel size being the smallest that enabled the whole sample to be scanned. Fig. 10(b) depicts the porosity scale distribution. The average pore diameter was calculated as 10.4 μm. The pores were observed to be approximately spherical. It was confirmed by the calculation of sphericity (Fig. 10(c)). The pores of the sintered sample were more spherical than the voids in the green sample. Small chains of pores in the green sample changed into closed pores in the sintered sample, which depicts complete sintering [42].

A tensile test was performed on the sintered sample with high density. Testing was also performed on the green sample in order to provide the strength of the 3D printed sample. The properties measured during the tensile test are shown in Table 2. The 3D printed green part consists of metal particles and binders to hold the metal particles. There was no physical bonding between the metal particles. Therefore, it resulted in poor mechanical properties. Fig. 11(a) and (b) show the SEM image of the green sample fracture. The small size dimples could be due to brittle

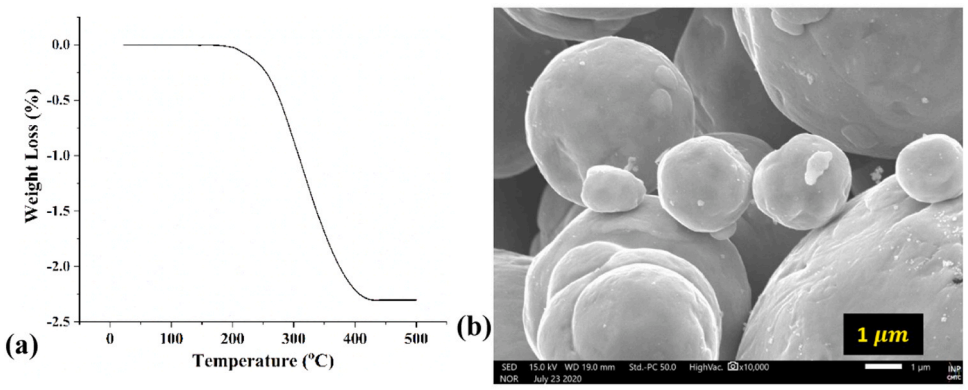

Fig. 7. (a) Solvent debinded sample weight loss through TGA and (b) SEM view of the sample after TGA.

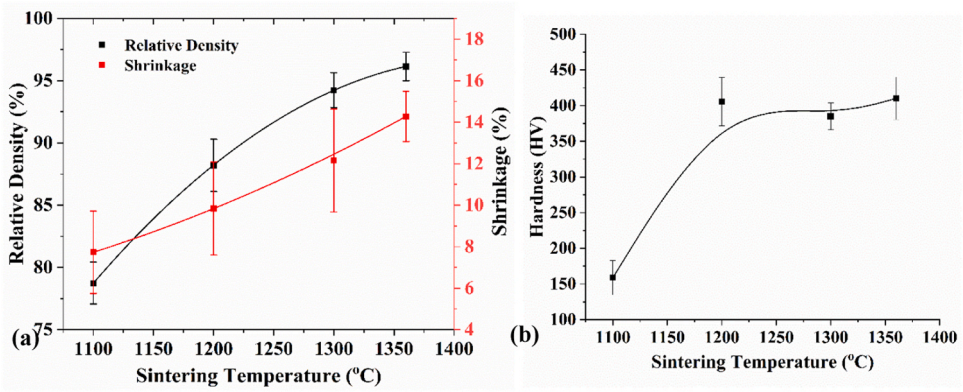

Fig. 8. (a) Change in density and shrinkage, and (b) hardness with respect to sintering temperature.

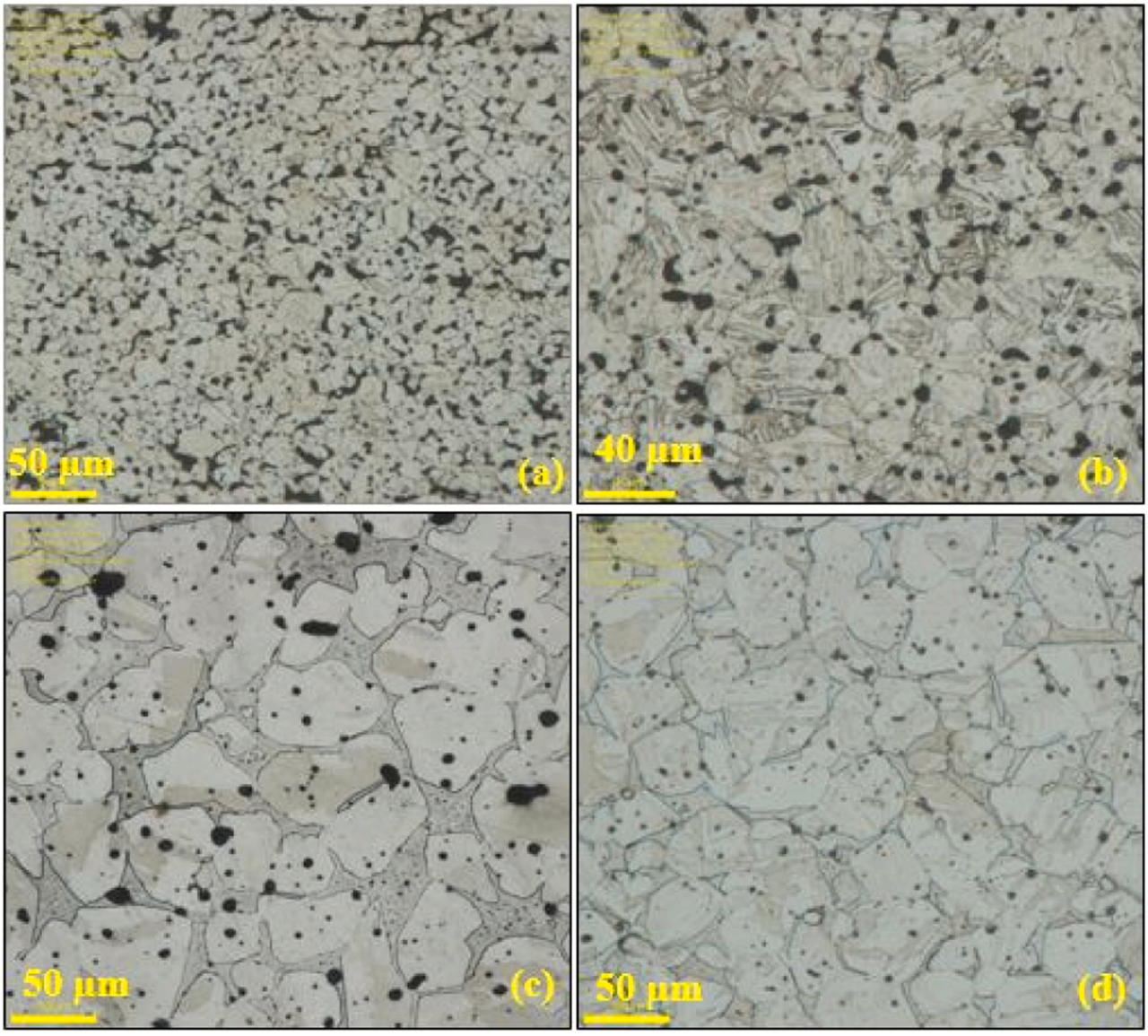

Fig. 9. Microstructure of the samples sintered at (a) 1100 ℃, (b) 1200 ℃, (c) 1300 ℃ and (d) 1360 ℃.

fracture of the binders.

The sintered sample with 96.5% relative density resulted in ~940 MPa tensile strength. The δ-ferrite reduced the porosity in the sample and improved the bonding. It resulted in higher tensile strength. Fig. 11(c) and (d) depict the fractured images of the sintered sample. It exhibits dimple ruptures with 5–15 µm size. A similar observation of tensile test results was observed by Gülsoy et al. [43] and Sung et al. [45] for 17–4PH MIM sintered parts studies.

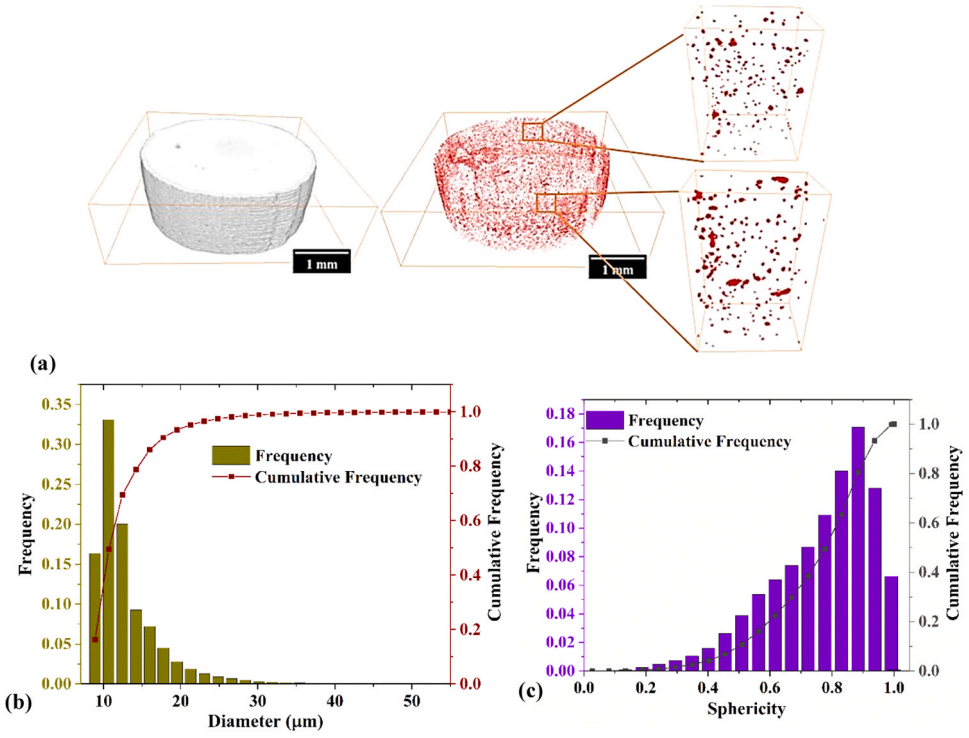

Fig. 10. (a) 3D rendering construction of tomography data, (b) pore size distribution and (c) sphericity distribution.

Table 2
Mechanical properties of the 3DEP green and sintered sample.

Sample	Young's modulus (GPa)	Yield Strength (MPa)	Ultimate Tensile Stress (MPa)	Strain at UTS (%)	Stress at break (MPa)	Strain at break (%)
Green	7.2	6.31	9.41	1.68	8.65	1.77
Sintered	112.4	822.7	939.5	2.53	831.092	3.67

4. Comparison with literature

FFF has been developed as a simple, secure, and low-cost alternative to traditional AM metal techniques for printing metal samples as a 3D extrusion printing (3DEP) process of metals combined with sintering. However, the performance of the fabricated samples must compete with other fabrication methods. For the sake of comparison, the present study results are compared with different AM and MIM processes (Table 3). The different properties such as density, surface roughness, hardness and ultimate tensile strength were compared to check the efficacy of the present work. Samples fabricated for 3D extrusion printing were found to have low density and tensile strength and approximate similar hardness value as compared to other AM process results such as Electron Beam Melting (EBM), Selective Laser Melting (SLM), Laser Engineering Net Shaping (LENS) and Wire Arc Additive Manufacturing (WAAM). It is due to the primary difference in the microstructure build-up mechanism. However, the present method is more cost-effective than other AM processes (Table 4). It is not only inexpensive in terms of capital investment, but it is also inexpensive in terms of the overall product cost. Tosto et al.[46] performed a cost modeling analysis between 3DEP and the SLM method. For a single product cost, 3DEP outperformed SLM by utilizing only 246.13 € as compared to 1147.88 €. However, production time analysis is also required for estimating overall productivity. Also, the 3DEP process outperformed other AM processes in terms of surface roughness. The present study results were similar to other 3DEP studies based on a metal-polymer filament. However, the machine cost for the present study is less than other market-available 3DEP popular machines (Table 4). Also, the utilization of MIM granules for 3D printing reduces the material cost and provide better handling. MIM feedstock products are less expensive because they are manufactured in vast amounts. They are more reliable because they have been engineered in binders and metal particle properties to deliver highly densified products by sintering. On the other hand, another 3DEP method necessitates special metal filaments, which raises the production expense. The findings of this study were also comparable to those of Metal Injection Molding (MIM). The method could reduce the cost and time spent preparing dies for the MIM operation, and it could also be used to fabricate parts in batch manufacturing with expert precision. Thermal treatments may also be used to enhance results.

5. Conclusion

Market available metal injection molding (MIM) feedstock of SS 17–4 PH was utilized as raw material for additive manufacturing. To achieve maximum sintered density, 3D printing, debinding, and sintering were thoroughly investigated. The conclusions drawn from the study are given below:

- 3D extrusion printing (3DEP) fabricated green samples resulted in ~4.911 g/cm^3 green density and a 2.8 μm surface roughness. Tomography study revealed the involvement of micron-sized voids in green body with ~13 μm diameter, which are almost difficult to remove.
- After 12 h of immersion in water at 60 °C, a net weight loss of 4.4% was observed during solvent debinding. During thermal debinding, the interconnected voids created by solvent debinding helps to eliminate backbone polymer. Also, TGA verified the complete removal of PEG during solvent debinding. After the complete debinding process, the gross weight loss was 6.8%.
- The sintered samples at 1360 °C for 3 h resulted in a maximum density of ~96.5% density and around ~14.1% shrinkage. The average diameter of ~10.4 μm porosity was evaluated using μCT

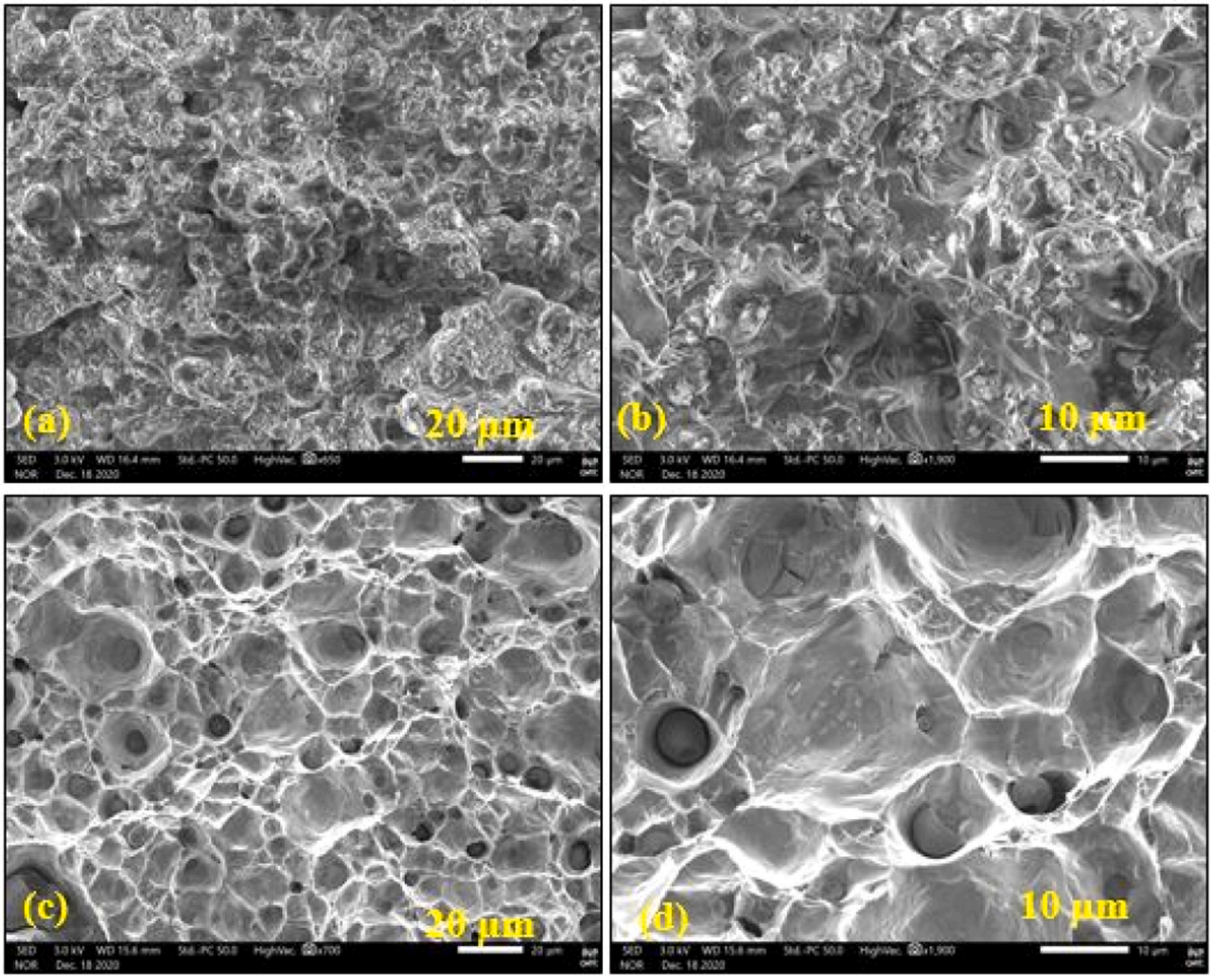

Fig. 11. (a, b) SEM images of the tensile fracture of 3D printed sample and (c, d) sintered sample at different magnifications.

Table 3
Comparison of present study properties with available literature.

Sr. No.	Fabrication technique	Material form	Powder size (μm)	Sintering temperature (°C)	Relative density (%)	Surface roughness (μm)	Hardness (HV)	Tensile strength (MPa)	Reference
1	3DEP	MIM granules	2–10	1360	95.8–97.1	2.7 – 3.6	380–440	940	Present
2	3DEP	Metal polymer filament	–	–	88.3–90.2	9.1 – 9.5	–	–	[47]
3	3DEP	Metal polymer filament	4.2 – 28.2	1380	94.2–96.1	–	–	666–1026	[17]
4	3DEP	Metal polymer filament	–	1300	91.4–96.2	–	–	–	[48]
5	3DEP	Metal polymer filament	4–28.2	1380	96–97	–	285	1050	[49]
6	3DEP	Metal polymer filament	–	–	–	–	–	467–512	[46]
7	Binder jetting 3D printing	Powder	–	–	96–99	3–12	340	1070–1200	[50]
8	LENS	Powder	45–90	–	97.2–98.1	–	350–420	–	[51]
9	EBM	Powder	–	–	99.6	16–31	320–385	1020–1230	[52]
10	SLM	Powder	–	–	Approx. 100	20.39–28.94	349–381	–	[53]
11	SLM	Powder	–	–	Approx. 100	–	280–320	1050–1150	[54]
12	WAAM	Welding wire	–	–	–	–	300–460	979–1009	[55]
13	MIM	MIM granules	10	1350	99	–	–	990–1050	[45]
14	MIM	MIM granules	60	1340	93.8	–	328	1020	[56]
15	MIM	MIM granules	–	1380	91.3 – 94.8	–	380–420	–	[44]
16	MIM	MIM granules	3.78 – 17.25	1350	95.9–96.2	–	–	1129–1143	[43]
17	MIM	MIM granules	11	1350	94.4–96	–	282–286	800	[57]

Table 4
Cost Comparison of popular AM machines.

Sr. No.	Company	Technique	Material Form	Cost (USD $)	Reference
1	AIM 3D	3DEP	MIM granules	50,000–100,000	[58]
2	Desktop metal	3DEP	Metal polymer filament	>150,000	[59]
3	Markforged metal X	3DEP	Metal polymer filament	150,000–200,000	[60]
4	ExOne M-flex 3D printer	Binder Jetting	Powder	>450,000	[61]
5	EOS M 400–4	SLM	Powder	>250,000	[62]
6	Arcam EBM spectra l GE additive	EBM	Powder	>250,000	[63]

analysis of the high-density sample. The shape of the pores was spherical in nature, characteristic of the final stage of sintering. The surface roughness of ~3.6 μm was measured for the sintered sample.

- A maximum hardness of about 400HV was measured for the samples sintered above 1200 ℃. However, no significant change in hardness was observed beyond 1200 ℃. The tensile properties of the 3D printed green sample at optimized parameters and of the sintered sample with high density were measured. The green sample resulted in low mechanical properties due to insufficient bonding between the mechanical particles. However, the sintered sample resulted in ~939.5 MPa tensile strength and the fracture surface exhibits dimples of size 5–15 μm.
- The present study results were compared to MIM and other AM processes results. The performance was closely similar to the MIM process. The surface roughness is far better than samples fabricated by SLM and EBM. Also, the process is more cost productive as compared to other AM processes.

The method has shown the application of MIM feedstock for 3DEP and sintering to acquire high solid density. However, the processing time is the limitation for this method of AM. As the future direction, the solvent and sintering steps processing time could be reduced by applying other innovative techniques. The water solvent method could replace petroleum-based solvent debinding or supercritical debinding method using CO_2 gas [64]. Different sintering methods such as microwave sintering [65], ultrasonic sintering [66] and field-assisted sintering [67] could be implemented during the sintering stage. These debinding and sintering methods could reduce the overall process time.

CRediT authorship contribution statement

Gurminder Singh: Conceptualization, Methodology, Investigation, Software, Writing – original draft. **Jean-Michel Missiaen**: Conceptualization, Supervision, Validation, Writing – review & editing. **Didier Bouvard**: Supervision, Visualization, Writing – reviewing & editing. **Jean-Marc Chaix**: Supervision, Resources, Writing – review & editing.

Declaration of Competing Interest

The authors declare that they have no known competing financial interests or personal relationships that could have appeared to influence the work reported in this paper.

Acknowledgements

Open Access funding provided by the IReL Consortium. The authors thank the Institute Carnot Energies du Future and Labex CEMAM for their significant contribution to the funding of this work (19T23 - IMPRIMEL). The authors thank University College Dublin, Ireland for the help.

References

[1] S. Singh, G. Singh, C. Prakash, S. Ramakrishna, Current status and future directions of fused fi lament fabrication, J. Manuf. Process. 55 (2020) 288–306, https://doi.org/10.1016/j.jmapro.2020.04.049.
[2] M. Montani, A.G. Demir, E. Mostaed, M. Vedani, B. Previtali, Process. Pure Zn Pure Fe SLM Biodegrad. Met. (2017), https://doi.org/10.1108/RPJ-08-2015-0100.
[3] D.A. Ramirez, L.E. Murr, E. Martinez, D.H. Hernandez, J.L. Martinez, B. I. MacHado, F. Medina, P. Frigola, R.B. Wicker, Novel precipitate-microstructural architecture developed in the fabrication of solid copper components by additive manufacturing using electron beam melting, Acta Mater. 59 (2011) 4088–4099, https://doi.org/10.1016/j.actamat.2011.03.033.
[4] A. Yegyan, Y. Bai, A. Eklund, C.B. Williams, The effects of hot isostatic pressing on parts fabricated by binder jetting additive manufacturing, Addit. Manuf. 24 (2018) 115–124, https://doi.org/10.1016/j.addma.2018.09.021.
[5] A. Mostafaei, E.L. Stevens, J.J. Ference, D.E. Schmidt, M. Chmielus, Binder jetting of a complex-shaped metal partial denture framework, Addit. Manuf. 21 (2018) 63–68, https://doi.org/10.1016/j.addma.2018.02.014.
[6] G. Singh, P.M. Pandey, Experimental investigations into mechanical and thermal properties of rapid manufactured copper parts, Proc. Inst. Mech. Eng. Part C J. Mech. Eng. Sci. 234 (2020) 82–95, https://doi.org/10.1177/0954406219875483.
[7] G. Singh, P.M. Pandey, Ultrasonic assisted pressureless sintering for rapid manufacturing of complex copper components, Mater. Lett. 236 (2019) 276–280, https://doi.org/10.1016/j.matlet.2018.10.123.
[8] G. Singh, P.M. Pandey, Uniform and graded copper open cell ordered foams fabricated by rapid manufacturing: surface morphology, mechanical properties and energy absorption capacity, Mater. Sci. Eng.: A 761 (2019), 138035, https://doi.org/10.1016/j.msea.2019.138035.
[9] G. Singh, P.M. Pandey, Topological ordered copper graphene composite foam: fabrication and compression properties study, Mater. Lett. 257 (2019) 1–5, https://doi.org/10.1016/j.matlet.2019.126712.
[10] X. Liu, B. Zou, H. Xing, C. Huang, The preparation of ZrO2-Al2O3 composite ceramic by SLA-3D printing and sintering processing, Ceram. Int. 46 (2020) 937–944, https://doi.org/10.1016/j.ceramint.2019.09.054.
[11] T. Zhou, L. Zhang, Q. Yao, Y. Ma, C. Hou, B. Sun, C. Shao, P. Gao, H. Chen, SLA 3D printing of high quality spine shaped β-TCP bioceramics for the hard tissue repair applications, Ceram. Int. 46 (2020) 7609–7614, https://doi.org/10.1016/j.ceramint.2019.11.261.
[12] Q. Chen, B. Zou, Q. Lai, Y. Wang, R. Xue, H. Xing, X. Fu, C. Huang, P. Yao, A study on biosafety of HAP ceramic prepared by SLA-3D printing technology directly, J. Mech. Behav. Biomed. Mater. 98 (2019) 327–335, https://doi.org/10.1016/j.jmbbm.2019.06.031.
[13] K. Rane, S. Petrò, M. Strano, Evolution of porosity and geometrical quality through the ceramic extrusion additive manufacturing process stages, Addit. Manuf. 32 (2020), 101038, https://doi.org/10.1016/j.addma.2020.101038.
[14] A.T. Sidambe, I.A. Figueroa, H.G.C. Hamilton, I. Todd, Metal injection moulding of CP-Ti components for biomedical applications, J. Mater. Process. Tech. 212 (2012) 1591–1597, https://doi.org/10.1016/j.jmatprotec.2012.03.001.
[15] L. Ren, X. Zhou, Z. Song, C. Zhao, Q. Liu, J. Xue, X. Li, Process parameter optimization of extrusion-based 3D metal printing utilizing PW-LDPE-SA binder system, Mater. (Basel) 10 (2017), https://doi.org/10.3390/ma10030305.
[16] J. Gonzalez-Gutierrez, D. Godec, C. Kukla, T. Schlauf, C. Burkhardt, C. Holzer, Shaping, debinding and sintering of steel components via fused filament fabrication, in: Proceedings of the 16th Int. Sci. Conf. Prod. Eng. - CIM2017. 2017.
[17] J. Gonzalez-Gutierrez, F. Arbeiter, T. Schlauf, C. Kukla, C. Holzer, Tensile properties of sintered 17-4PH stainless steel fabricated by material extrusion additive manufacturing, Mater. Lett. 248 (2019) 165–168, https://doi.org/10.1016/j.matlet.2019.04.024.
[18] K. Rane, K. Castelli, M. Strano, Rapid surface quality assessment of green 3D printed metal-binder parts, J. Manuf. Process. 38 (2019) 290–297, https://doi.org/10.1016/j.jmapro.2019.01.032.
[19] Y. Thompson, J. Gonzalez-Gutierrez, C. Kukla, P. Felfer, Fused filament fabrication, debinding and sintering as a low cost additive manufacturing method of 316L stainless steel, Addit. Manuf. 30 (2019), 100861, https://doi.org/10.1016/j.addma.2019.100861.
[20] X. Yan, L. Hao, W. Xiong, D. Tang, Research on influencing factors and its optimization of metal powder injection molding without mold via an innovative 3D printing method, RSC Adv. 7 (2017) 55232–55239, https://doi.org/10.1039/c7ra11271h.
[21] D. Godec, S. Cano, C. Holzer, J. Gonzalez-Gutierrez, Optimization of the 3D printing parameters for tensile properties of specimens produced by fused filament fabrication of 17-4PH stainless steel, Mater. (Basel) 13 (2020), https://doi.org/10.3390/ma13030774.
[22] T.C. Henry, M.A. Morales, D.P. Cole, C.M. Shumeyko, J.C. Riddick, Mechanical behavior of 17-4 PH stainless steel processed by atomic diffusion additive manufacturing, Int. J. Adv. Manuf. Technol. 114 (2021) 2103–2114, https://doi.org/10.1007/s00170-021-06785-1.

[23] K. Rane, S. Cataldo, P. Parenti, L. Sbaglia, V. Mussi, M. Annoni, M. Strano, K. Rane, S. Cataldo, P. Parenti, L. Sbaglia, Rapid Production of Hollow SS316 Profiles By Extrusion Based Additive Manufacturing, 140014, 2018. https://doi.org/10.1063/1.5035006.

[24] K. Rane, L. Di Landro, M. Strano, Processability of SS316L powder - binder mixtures for vertical extrusion and deposition on table tests, Powder Technol. 345 (2019) 553–562, https://doi.org/10.1016/j.powtec.2019.01.010.

[25] C. Kukla, S. Cano, D. Kaylani, S. Schuschnigg, C. Holzer, J. Gonzalez-Gutierrez, Debinding behaviour of feedstock for material extrusion additive manufacturing of zirconia, Powder Met. 62 (2019) 196–204, https://doi.org/10.1080/00325899.2019.1616139.

[26] K. Rane, M.A. Farid, W. Hassan, M. Strano, Effect of printing parameters on mechanical properties of extrusion-based additively manufactured ceramic parts, Ceram. Int. (2021) 1–10, https://doi.org/10.1016/j.ceramint.2021.01.066.

[27] M. Galati, P. Minetola, Analysis of density, roughness, and accuracy of the atomic diffusion additive manufacturing (ADAM), Materials (Basel) (2019).

[28] A. Bose, C.A. Schuh, J.C. Tobia, N. Tuncer, N.M. Mykulowycz, A. Preston, A. C. Barbati, B. Kernan, M.A. Gibson, D. Krause, T. Brzezinski, J. Schroers, R. Fulop, J.S. Myerberg, M. Sowerbutts, Y.M. Chiang, A. John Hart, E.M. Sachs, E.E. Lomeli, A.C. Lund, Traditional and additive manufacturing of a new Tungsten heavy alloy alternative, Int. J. Refract. Met. Hard Mater. 73 (2018) 22–28, https://doi.org/10.1016/j.ijrmhm.2018.01.019.

[29] G. Singh, J.M. Missiaen, D. Bouvard, J.M. Chaix, Copper extrusion 3D printing using metal injection moulding feedstock: analysis of process parameters for green density and surface roughness optimization, Addit. Manuf. 38 (2021), 101778, https://doi.org/10.1016/j.addma.2020.101778.

[30] G. Singh, J. Missiaen, D. Bouvard, J. Chaix, Copper additive manufacturing using MIM feedstock: adjustment of printing, debinding, and sintering parameters for processing dense and defectless parts, Int. J. Adv. Manuf. Technol. 115 (2021) 449–462, https://doi.org/10.1007/s00170-021-07188-y.

[31] W. Lengauer, I. Duretek, M. Fürst, V. Schwarz, J. Gonzalez-Gutierrez, S. Schuschnigg, C. Kukla, M. Kitzmantel, E. Neubauer, C. Lieberwirth, V. Morrison, Fabrication and properties of extrusion-based 3D-printed hardmetal and cermet components, Int. J. Refract. Met. Hard Mater. 82 (2019) 141–149, https://doi.org/10.1016/j.ijrmhm.2019.04.011.

[32] A.T. Sidambe, I. Todd, P. Hatton, Effect of processing parameters on the properties of metal injection moulded titanium dental implants, Mater. Sci. Forum 828–829 (2015) 145–151, https://doi.org/10.4028/www.scientific.net/MSF.828-829.145.

[33] L. Ammosova, S. Cano Cano, S. Schuschnigg, C. Kukla, K. Mönkkönen, M. Suvanto, J. Gonzalez-Gutierrez, Effect of metal particle size and powder volume fraction on the filling performance of powder injection moulded parts with a microtextured surface, Precis. Eng. 72 (2021) 604–612, https://doi.org/10.1016/j.precisioneng.2021.06.014.

[34] M.M. Shbeh, A. Yerokhin, R. Goodall, Microporous titanium through metal injection moulding of coarse powder and surface modification by plasma oxidation, Appl. Sci. 7 (2017), https://doi.org/10.3390/app7010105.

[35] C. Duty, C. Ajinjeru, V. Kishore, B. Compton, N. Hmeidat, X. Chen, P. Liu, A. A. Hassen, J. Lindahl, V. Kunc, What makes a material printable? A viscoelastic model for extrusion-based 3D printing of polymers, J. Manuf. Process. 35 (2018) 526–537, https://doi.org/10.1016/j.jmapro.2018.08.008.

[36] Y. Sugiyama, M. Hazama, N. Iwakami, Device and method for the extrusion of thermo - mechanically deformable materials in bulk form, and compact screw extruder, US Pat. Appl. 2020 (2005) 1–24. ⟨http://www.freepatentsonline.com/y2005/0234116.html⟩.

[37] V. Boulos, V. Fristot, D. Houzet, L. Salvo, P. Lhuissier, Investigating performance variations of an optimized GPU-ported granulometry algorithm To cite this version: HAL Id: hal-00787861 Investigating performance variations of an optimized GPU-ported granulometry algorithm, Des. Archit. Signal Image Process. (2012) 1–6.

[38] J.R. Davis, Stainless steels, ASM international,, 1994.

[39] Y. Wu, R.M. German, D. Blaine, B. Marx, C. Schlaefer, Effects of residual carbon content on sintering shrinkage, microstructure and mechanical properties of injection molded 17-4 PH stainless steel, J. Mater. Sci. 7 (2002) 3573–3583.

[40] Y. Wu, D. Blaine, B. Marx, C. Schlaefer, R.M. German, Sintering densification and microstructural evolution of injection molding grade 17-4 PH stainless steel powder, Metall. Mater. Trans. A Phys. Metall. Mater. Sci. 33 (2002) 2185–2194.

[41] I.M. Fedorchenko, V.V. Skorokhod, Theory and practice of sintering, Sov. Powder Metall. Met. Ceram. 6 (1967) 790–805, https://doi.org/10.1007/BF00773720.

[42] R. German, Sinter.: Empir. Obs. Sci. Princ. (2014), https://doi.org/10.1016/C2012-0-00717-X.

[43] H.Ö. Gülsoy, S. Özbek, T. Baykara, Microstructural and mechanical properties of injection moulded gas and water atomised 17-4 PH stainless steel powder, Powder Met. 50 (2007) 120–126, https://doi.org/10.1179/174329007×153288.

[44] B. Suharno, D. Ferdian, H. Restucondro, L. Pradinda, E.R. Baek, S. Supriadi, Vacuum sintering process in metal injection molding for 17–4 ph stainless steel as material for orthodontic bracket, Solid State Phenom. 266 (2017) 231–237, https://doi.org/10.4028/www.scientific.net/SSP.266.231.

[45] H.J. Sung, T.K. Ha, S. Ahn, Y.W. Chang, Powder injection molding of a 17-4 PH stainless steel and the effect of sintering temperature on its microstructure and mechanical properties, J. Mater. Process. Technol. 130–131 (2002) 321–327, https://doi.org/10.1016/S0924-0136(02)00739-2.

[46] C. Tosto, J. Tirillò, F. Sarasini, G. Cicala, Hybrid metal/polymer filaments for fused filament fabrication (FFF) to print metal parts, Appl. Sci. 11 (2021) 1444, https://doi.org/10.3390/app11041444.

[47] M. Galati, P. Minetola, Analysis of density, roughness, and accuracy of the atomic diffusion additive manufacturing (ADAM) process for metal parts, Materials 12 (2019) 4122, https://doi.org/10.3390/ma1224122.

[48] C. Lieberwirth, M. Sarhan, H. Seitz, Mechanical properties of stainless-steel structures fabricated by composite extrusion modelling, Metals 8 (2018) 84, https://doi.org/10.3390/met8020084.

[49] A.I. Nurhudan, S. Supriadi, Y. Whulanza, A.S. Saragih, Additive manufacturing of metallic based on extrusion process: A review, J. Manuf. Process. 66 (2021) 228–237, https://doi.org/10.1016/j.jmapro.2021.04.018.

[50] ExOne, 17–4PH Stainless Steel, (2012) 2012. ⟨http://www.exone.com/Portals/0/ResourceCenter/Materials/PSC_X1_MaterialData_17–4_SS_US_012018.pdf⟩.

[51] I. Mathoho, E.T. Akinlabi, N. Arthur, M. Tlotleng, N.W. Makoana, The effects of LENS process parameters on the behaviour of 17-4 PH stainless steel, Miner. Met. Mater. Ser. (2020) 481–490, https://doi.org/10.1007/978-3-030-36296-6_45.

[52] P. Chemistry, S. Plot, T. States, Ge 17–4 Ph, (n.d.) 1–2.

[53] P. Ponnusamy, S.H. Masood, S. Palanisamy, R.A. Rahman Rashid, D. Ruan, Characterization of 17-4 PH alloy processed by selective laser melting, Mater. Today Proc. 4 (2017) 8498–8506, https://doi.org/10.1016/j.matpr.2017.07.196.

[54] B. Laserform, P. Dmp, D.M. Printers, Laser ® 17-4PH (B) (2017) 300.

[55] A. Caballero, J. Ding, S. Ganguly, S. Williams, Wire + Arc Additive Manufacture of 17-4 PH stainless steel: effect of different processing conditions on microstructure, hardness, and tensile strength, J. Mater. Process. Technol. 268 (2019) 54–62, https://doi.org/10.1016/j.jmatprotec.2019.01.007.

[56] J. Kazior, A. Szewczyk-Nykiel, T. Pieczonka, M. Hebda, M. Nykiel, Properties of precipitation hardening 17-4 PH stainless steel manufactured by powder metallurgy technology, Adv. Mater. Res. 811 (2013) 87–92, https://doi.org/10.4028/www.scientific.net/AMR.811.87.

[57] J. Shi, Z. Cheng, J.C. Gelin, T. Barriere, B. Liu, Sintering of 17-4PH stainless steel powder assisted by microwave and the gradient of mechanical properties in the sintered body, Int. J. Adv. Manuf. Technol. 91 (2017) 2895–2906, https://doi.org/10.1007/s00170-016-9960-y.

[58] ⟨https://www.aniwaa.com/product/3d-printers/aim3d-exam-255/⟩, (n.d.).

[59] ⟨https://www.desktopmetal.com/press/press-release—desktop-metal-launches-worlds-first-metal-binder-jetting-system-for-machine-shops⟩, (n.d.).

[60] ⟨https://markforged.com/resources/blog/metal-x-roi⟩, (n.d.).

[61] ⟨https://www.engineering.com/story/exone-m-flex-production-metal-3d-printer⟩, (n.d.).

[62] ⟨https://www.aniwaa.com/product/3d-printers/eos-eos-m-400–4/⟩, (n.d.).

[63] ⟨https://www.aniwaa.com/product/3d-printers/ge-additive-arcam-ebm-spectra-l/⟩, (n.d.).

[64] A. Royer, T. Barriere, Y. Bienvenu, Influence of supercritical debinding and processing parameters on final properties of injection-moulded Inconel 718, Powder Technol. 336 (2018) 311–317, https://doi.org/10.1016/j.powtec.2018.05.047.

[65] D. Demirskyi, D. Agrawal, A. Ragulya, Neck growth kinetics during microwave sintering of copper, Scr. Mater. 62 (2010) 552–555, https://doi.org/10.1016/j.scriptamat.2009.12.036.

[66] G. Singh, P.M. Pandey, Rapid manufacturing of copper components using 3D printing and ultrasonic assisted pressureless sintering: experimental investigations and process optimization, J. Manuf. Process. 43 (2019) 253–269, https://doi.org/10.1016/j.jmapro.2019.05.010.

[67] M. Biesuz, D. Rizzi, V.M. Sglavo, Electric current effect during the early stages of field-assisted sintering, J. Am. Ceram. Soc. 102 (2019) 813–822, https://doi.org/10.1111/jace.15976.